ACS EARTH AND SPACE CHEMISTRY

Open Access

http://pubs.acs.org/journal/aesccq

Article

Interactions of Urea Surfaces with Water as Relative Humidity Obtained from Dynamic Vapor Sorption Experiments, *In Situ* Single-Particle Raman Spectroscopy, and *Ab Initio* Calculations

Mohamed Eisa, Dovilė Ragauskaitė, Jingming Shi, Seishi Shimizu, Tomas Bucko, Clinton Williams, and Jonas Baltrusaitis*

Cite This: https://doi.org/10.1021/acsearthspacechem.3c00210

Read Online

ABSTRACT: Urea is a critical nitrogen carrier molecule that is abundant in the environment due to its anthropogenic activity to enhance crop growth. The intrinsic link between its high solubility and volatilization, resulting in the reactive nitrogen species and CO_2, especially under excessive relative humidity (RH) conditions, suggests that the urea hydrolysis-initiated decomposition reaction can be affecting the global nitrogen balance. Fundamental analysis of water as RH adsorption on urea particle surfaces was performed using a combination of dynamic vapor sorption (DVS) experiments, in situ single-particle Raman spectroscopy, and ab initio calculations. The DVS data acquired exhibited three RH adsorption regimes with urea with 74% RH dramatically changing adsorbate–urea interactions from monolayer- to multilayer-induced deliquescence. Several empirical kinetic models were utilized to understand the RH interaction with urea surfaces, and the Guggenheim–Anderson–de Boer model provided a good description of the adsorption at <60% RH values, while a Van Campen model was used to fit the data acquired during the urea crystal deliquescence. The experimental water sorption rate using the Van Campen model showed a gradual rise from 0.02 mg/min at 80% to 0.08 mg/min at 95% in agreement with Van Campen's model of increasing trend, albeit at higher rates ranging from 0.03 mg/min at 80% to 0.1 mg/min at 95%. In situ Raman spectroscopy combined with optical images of a single particle showed that the urea 1009 cm^{-1} peak full width at half-maximum can provide in-depth information on the transient phenomena taking place on the urea particle surface as well as in the partially liquefied environment. Finally, density functional theory results suggested that Wulff's reconstruction of a single urea crystal depended on the presence of higher crystalline planes; particularly, the (111) facet became significant together with (101) and (110), while in the presence of bulk H_2O, (101) became the dominant facet. The results presented in this work will allow for a better understanding of urea–water vapor interactions in the environment at the molecular level including its potential for aerosol formation in the regions of high agricultural activity. Further, this study will allow us to better understand urea partitioning into soil pore volume where high RH is prevalent. Finally, it will provide a microscopic, single-particle understanding of the urea transformations in moist environments and pave the way for a new, nitrogen-efficient material fertilizer design.

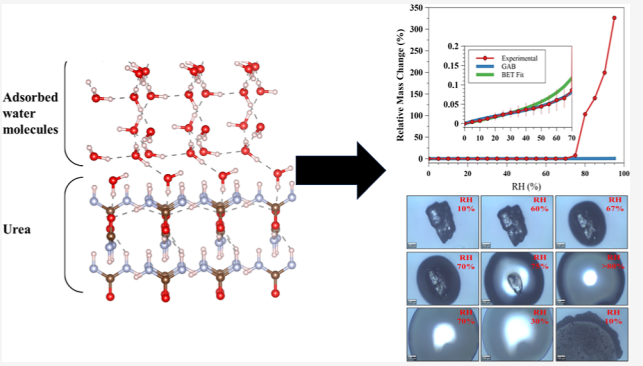

KEYWORDS: *urea, nitrogen, Raman, in situ, relative humidity, DFT*

INTRODUCTION

Urea (NH_2CONH_2) is a ubiquitous chemical compound that plays a vital role across various industries and daily living.[1,2] Due to the high nitrogen content, urea has quickly emerged as the most popular solid fertilizer with approximately 180–200 million metric tons of global demand in recent years.[3,4] The unique chemical structure of the urea molecule[5,6] results in a substantial polarity and a high capacity for forming hydrogen bonds,[7] resulting in its high solubility in water[8] as well as other polar solvents, including ethanol and methanol.[9,10] Generally, solubility is a key factor contributing to substance hygroscopicity and deliquescence at different relative humidity (RH) conditions as an increase in solubility leads to higher hygroscopicity[11] and lower RH needed for deliquescence to occur.[12] Consequently, urea is well known for its high

Received: July 17, 2023
Revised: September 1, 2023
Accepted: September 5, 2023

hygroscopicity and its ability to undergo deliquescence at high RH.[13−15] Moreover, RH is a critical factor in ammonia volatilization from urea.[16−23] It has been found that, on average, N losses resulting from the use of urea range from 20 to 33% and can be as high as 70% under excessive RH conditions,[24] thus potentially affecting the global nitrogen balance.

The persistent N losses often incentivize the overuse of fertilizers, causing a surplus of nutrients, notably nitrogen and phosphorus, within aquatic ecosystems. Such a surplus can lead to concerning environmental issues, such as eutrophication. Additionally, NH_4^+ resulting from urea hydrolysis is oxidized to NO_3^-, which further can be subjected to denitrifying bacteria, culminating in the release of reactive nitrogen compounds, for instance, N_2O. It is worth noting that the greenhouse gas potential of N_2O is approximately 300 times more potent than CO_2.[25−28] The implications of N loss extend beyond environmental concerns and intersect with energy pollution. Specifically, the production of NH_3, a precursor to urea, has been implicated in significant energy consumption accounting for an estimated 3−5% of the total yield from natural gas and between 1 and 2% of the world's energy resources.[29,30] Furthermore, due to the large influx of urea into the environment as a mineral fertilizer, it significantly contributes to the dissolved organic nitrogen in rainwater and aqueous aerosols.[31] As a prominent urea source within the aerosols, emissions from the cattle have also been proposed.[32] Recent studies have shown that up to 30% of the water-soluble organic nitrogen in a maritime aerosol can be derived from amino acids, amines, and urea.[33] However, a large discrepancy in the urea content in water-soluble aerosol organic nitrogen can be found in the literature ranging by 2 orders of magnitude.[34]

Given the ubiquity of urea and the corresponding issues related to N losses and environmental implications, it is significantly important to have an in-depth understanding of its interaction with water vapor. Preliminary literature suggests a degree of incompleteness in the current understanding of this interaction, hinting at the potential for further research and investigation of this subject. Water vapor interactions with urea were studied earlier under different RHs and showed that at 74% RH, deliquescence started to occur and referring to this RH level as the critical RH, and the maximum water uptake was around 150% of the sample dry weight.[14] When urea was equilibrated for approximately 2500 min at 81% RH, the water uptake was around 80% dry basis (d.b.),[14] likely underestimating the true water vapor sorption capacity of urea particles. Another study investigated the water vapor sorption on urea and aimed to determine the thickness of adsorbed water layers that alter the surface properties of urea.[35] However, the study did not focus on showing the water uptake at humidity >40% RH.[35] The water vapor isotherm of urea was also reported recently, and it also showed that the onset of deliquescence in urea was observed at 74% RH.[36] It was shown that as the humidity increased, the water vapor gradually condensed, diluting the condensate and enabling more urea solids to dissolve.[36] The process of water uptake continues until the solid is fully dissolved and further solution dilution takes place.[36] It was shown in this study that the maximum water uptake at 95% RH was around 260%,[36] which is significantly higher than the value reported earlier (~150%[14]), and the accuracy of these measurements was likely affected by the time allotted to achieve equilibrium conditions.

While urea−water vapor interactions hold substantial relevance in numerous applications and can have significant implications for the atmospheric nitrogen balance, there exists a lack of fundamental information that interrogates how water as RH interacts with the urea particle surface at the molecular level. Furthermore, urea is not incorporated into prevalent aerosol thermodynamic models, such as E-AIM[37] and ISORROPIA II,[38] which have successfully modeled the behavior of other nitrogenous compounds, including ammonium sulfate[39] and ammonium nitrate.[40] The objective of this study is to undertake a comprehensive attempt to model the water vapor isotherm in conjunction with urea to better understand the fundamental interactions of water vapor and urea. In particular, we employ dynamic vapor sorption (DVS) experiments, in situ single-particle Raman spectroscopy, and ab initio calculations to interrogate urea−water vapor interactions at the molecular level.

MATERIALS AND METHODS

Urea powder was purchased from Sigma-Aldrich (99−100.5%) and used as received.

DVS Experiments. The DVS Intrinsic (surface measurement systems) was used for all DVS experiments. Urea powder (~20 mg) was loaded into the sample pan and exposed to dry airflow (medical grade, RH < 2%) for 24 h to remove weakly bound water from the surface. After the drying, the RH was increased from 0 to 95% and then decreased back to <2% in increments of 5%. During each cycle, the adsorbed mass was recorded as a function of time until the mass change rate (dm/dt) was under 0.002 mg/min where equilibrium was previously reported for high-deliquescence urea particles.[41] A probe in the sample chamber was used to constantly measure the temperature and maintain the temperature at a constant temperature of 25 °C. The SMS DVS Analysis Suite software package was used to perform data analysis functions such as baseline correction, isotherm calculation, and heat of sorption analysis. HPLC-grade water (Millipore-Sigma) was used in all of the DVS experiments.

Modeling Adsorption Isotherms. The Freundlich isotherm was initially used to understand water as RH interactions with urea surfaces at low RH values by transforming it into its linear form (eq 1)[42]

$$\log\left(\frac{x}{m}\right) = \log(K_f) + \frac{1}{n}\log\left(\frac{P}{P_o}\right) \quad (1)$$

where x and m represent the alteration in mass and the aggregate dry mass of the sample, respectively. Meanwhile, K_f refers to a constant associated with the Freundlich equilibrium, while the n term signifies a fitting coefficient that reflects the binding attraction on the surface of the adsorbent and P/P_o signifies the relative pressure of the adsorbing gas. It was applied in the two linear regions found in the $\frac{x}{m}$ vs $\frac{P}{P_o}$ plot, e.g., one in the low RH region (0−20%) and the second in the middle RH region (25−60%) before deliquescence occurred. While mostly empirical, the Freundlich adsorption model accounts for intermolecular interactions between adsorbates and implies heterogeneity of adsorption sites[43] but is only linear at low pressures.

The traditional BET (eq 2) was utilized to better represent multilayer adsorption within the RH range of 0.05−0.35 taking place before deliquescence of urea as eq 2 cannot precisely depict isotherms for RH values exceeding 0.5[44,45] but is widely used to describe the adsorbate behavior and quantity on the surface of the adsorbent.[46,47]

https://doi.org/10.1021/acsearthspacechem.3c00210
ACS Earth Space Chem. XXXX, XXX, XXX−XXX

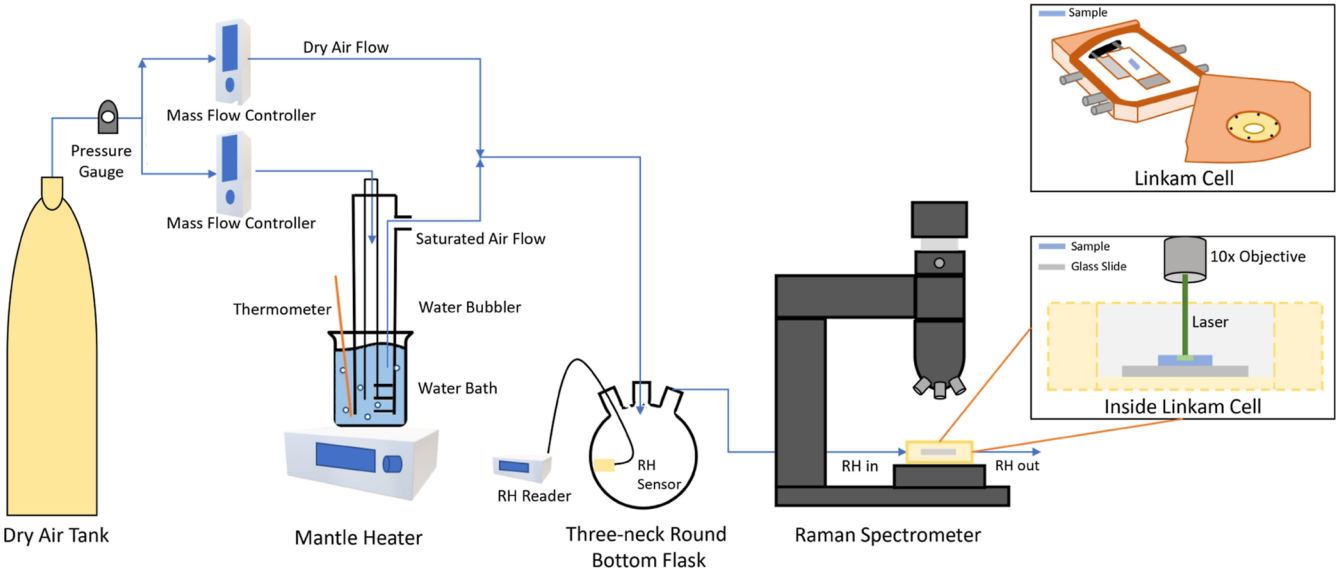

Figure 1. In situ Raman experimental setup to monitor urea single-particle reactions with RH.

$$\frac{1}{W\left(\frac{P_0}{P_i}-1\right)} = \frac{C-1}{W_m C}\times\frac{P_i}{P_0}+\frac{1}{W_m C} \tag{2}$$

as C is a dimensionless sorption constant that is exponentially related to the adsorption energy difference between the first and second layers.[48] W denotes the adsorbed amount of the adsorbate per mass of the sorbent (dry base) at equilibrium and W_m represents the monolayer capacity, while the relative pressure is represented by P/P_o, which can also be expressed by RH. The method used to compute the Guggenheim–Anderson–de Boer (GAB) fitting parameters was carried out in accordance with the literature.[49] The general formula of the GAB isotherm is as follows

$$\frac{W}{W_m} = \frac{CKa_w}{(1-Ka_w)[1+(C-1)Ka_w]} \tag{3}$$

where W represents the equilibrium water content (% dry-based), W_m is the monolayer water content, and a_w represents the water activity as $a_w = \frac{\mathrm{ERH}}{100}$, where ERH represents equilibrium RH. The parameters K and C are temperature dependent and expressed by Arrhenius-type equations, with associated molar sorption enthalpies.[49] Equation 3 can be written in a different form,[50] allowing the calculations of K, C, and W_m parameters

$$\frac{a_w}{W} = a + ba_w + ca_w^2 \tag{4}$$

where a, b, and c are functions of K, C, and W_m and can be obtained from the regression analysis of the $\frac{a_w}{W}$ vs a_w plot. The parameter K can then be obtained as the positive solution of the quadratic equation (eq 5)

$$0 = aK^2 + bK + c \tag{5}$$

while C and W_m can be calculated using eqs 6 and 7

$$C = \frac{b}{aK} + 2 \tag{6}$$

$$W_m = \frac{1}{b+2aK} \tag{7}$$

The regression analysis for eq 4 was performed using our Python-based software tools employing the poly1d class, as available in the numpy library.

Raman Spectroscopy. Raman spectra were acquired using a WITec alpha300R confocal Raman microscope using a 532 nm laser, Zeiss EC Epiplan-Neofluar 10×, G2:600 g/mm grating, and a 3 s integration time per point. The spectral range was 100–4000 cm^{-1} with the center at 2000 cm^{-1}, and the spectral resolution was ~2 cm^{-1}. Before each experiment, the instrument was calibrated using a Si wafer. The laser intensity of the sample was ~54 mW.

In situ RH adsorption measurements on a single urea particle were performed using a Linkam LTS 350 environmental cell operating at 23 °C, as shown in Figure 1. In particular, dry air was supplied via two mass flow controllers and a water bath saturator. The saturator was held at a constant temperature, and the mixed air containing water as RH was supplied into a three-neck round-bottom flask where RH values were recorded. Air then further passed into the environmental Linkam cell equipped with a quartz window. The accuracy of the RH sensor was ±2%.

Ab Initio Calculations. Periodic DFT calculations were performed as implemented in the VASP.[51−54] The projector-augmented wave (PAW) method of Blöchl,[55] as adapted by Kresse and Joubert,[56] was used to describe the effective interaction between the valence electrons and the core. The exchange–correlation energy was described by the spin-unpolarized version of the PBE functional[57] in combination with DFT-D2 dispersion correction by Grimme.[58,59] The Brillouin zone was sampled using 4 × 4 × 4 for urea bulk crystal. The Kohn–Sham equations were solved self-consistently in a plane-wave basis set with a cutoff of 400 eV. The convergence criterion for the electronic self-consistency cycle, measured by the change in the total energy between successive iterations, was set to 10^{-6} eV per unit cell.

Initial crystalline unit cell parameters for structural optimization were obtained from the literature for urea.[60] A series of constant volume relaxations was performed to

https://doi.org/10.1021/acsearthspacechem.3c00210
ACS Earth Space Chem. XXXX, XXX, XXX−XXX

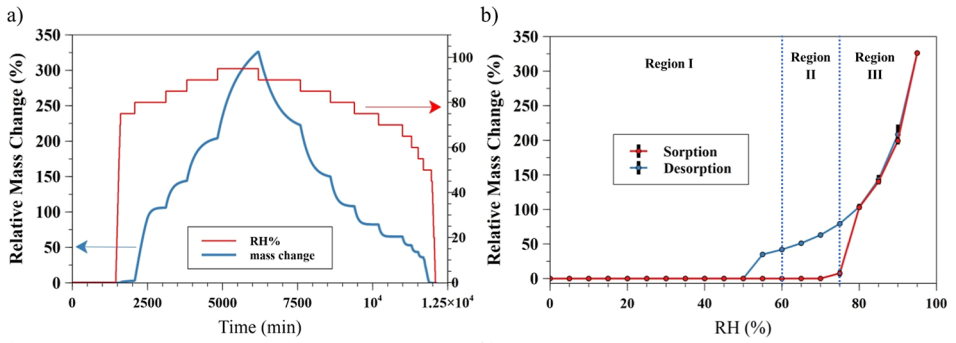

Figure 2. Water−urea sorption data before deliquescence: (a) water relative mass change with urea as RH changes and (b) water isotherm on urea.

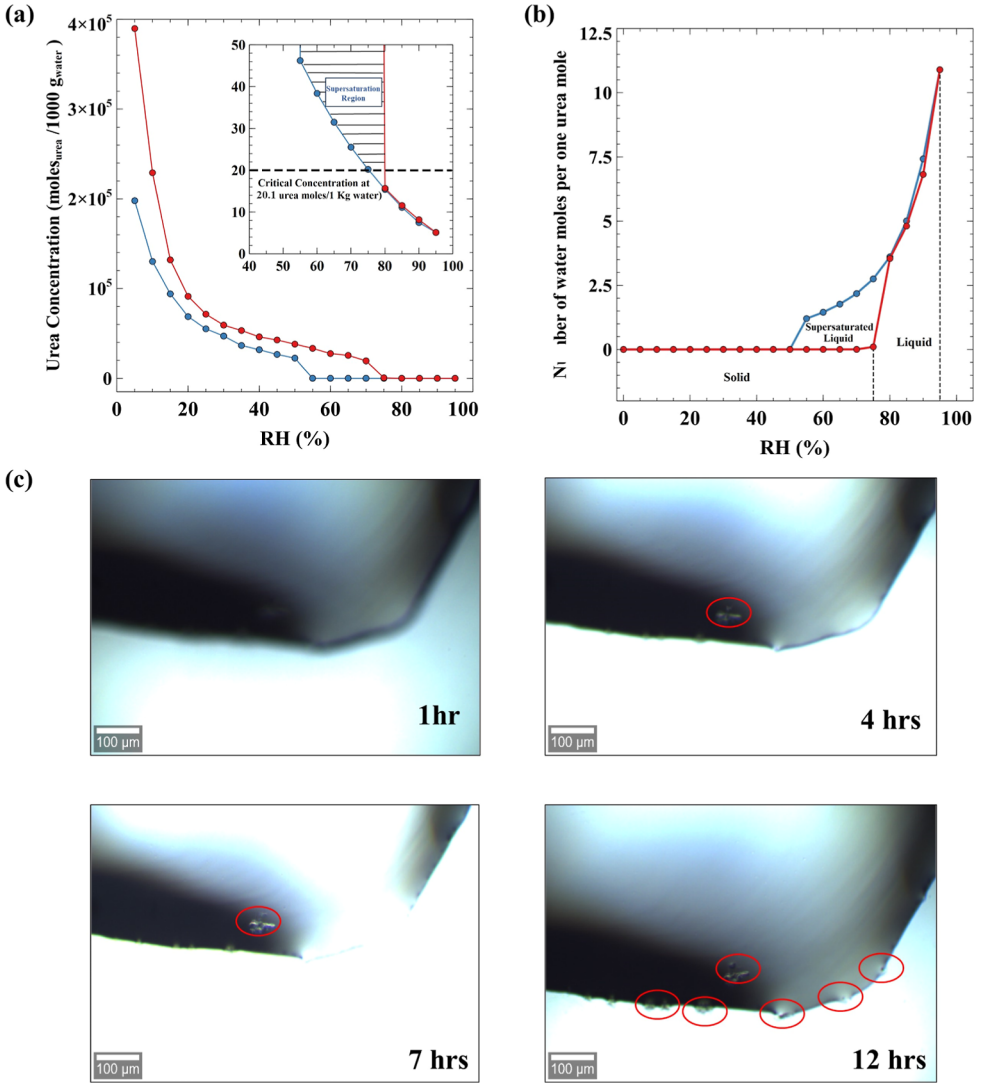

Figure 3. (a) Urea concentration in water adsorbed over RH with an emphasis on the hysteresis onset region, indicating supersaturation; (b) transformation of urea across various phases in response to changes in RH; and (c) optical images of deliquescent urea during a desorption cycle at a steady RH of 50%, revealing time-dependent crystallization patterns.

determine the ground-state volume (V_0) of the crystal from fit to the Murnaghan equation of state.[61] Last, one more constant volume relaxation of atomic positions was performed for the structure with V_0, and the resulting structures were used in ab initio thermodynamic analyses. Surface slabs were created for (001), (110), (101), (111), and (200) surface terminations of urea for various thicknesses of the slabs. (001) possessed molecular urea unit orientation perpendicular to the surface plane with $-NH_2$ moieties oriented toward the vacuum. (110) contained urea units perpendicular to each other, while (101), (111), and (200) had complex orientation with C═O moieties also oriented toward vacuum. The thickness of the slab for each termination was converged until the energy change with thickness was negligible. The surface energy of the slab

https://doi.org/10.1021/acsearthspacechem.3c00210
ACS Earth Space Chem. XXXX, XXX, XXX−XXX

consisting of n formula units (γ) was calculated according to eq 8.

$$\gamma = \frac{E_n - nE_{bulk}}{2A} \quad (8)$$

where E_{bulk} is the bulk crystal energy per formula unit and A is the surface area of the unit slab. To simulate solvated urea surfaces, the ab initio molecular dynamics (AIMD) calculation *NVT* ensemble was performed using an Andersen thermostat[62] (296 K and 1 fs steps) to provide sufficient kinetic energy to the simulated urea surface-adsorbed water molecule. Similarly, adsorption of one molecular monolayer was considered in relaxations of the (001), (110), (101), (111), and (200) surface slabs. Additionally, the vacuum space above the surface slab was filled with the explicit bulk water molecules corresponding to 55 molar H_2O at bulk water density. The state with the lowest energy identified was again relaxed by using PBE-D2. The lowest energy shape of the crystals under vacuum and solvated conditions was constructed using Wulff[63] construction via the Python-based WulffPack code.[64]

RESULTS

Urea Particle Interactions with RH Using DVS Measurements. Figure 2 illustrates the hygroscopic behavior of urea particles via adsorption and desorption isotherms with raw relative mass change data in Figure 2a and calculated sorption/desorption branches in Figure 2b. As per the categorization by Brunauer,[65] the urea RH sorption isotherm is identified as type III. The sorption isotherm of urea can be partitioned into three primary sections. The first region (0% < RH < 60%) signifies strongly bound water with the water molecules in this area being considered monolayer water. These molecules are tightly linked with hydrophilic urea and polar groups (−OH and $-NH_2$). The subsequent region (60% < RH < 74%) denotes water with a weaker binding, categorized as multilayer water. In this section, water is retained within urea's solid structure through capillary condensation, and its vaporization enthalpy is marginally greater than that of pure water.[66,67] The third region (RH > 74%) demonstrates urea going through deliquescence, as free water is found in a solvent-like state[68] dissolving urea. Adsorbed water properties in this area closer resemble those of bulk water, allowing the water to act as a solvent and be accessible for chemical reactions with urea molecules.[69] It can be observed that a higher RH (RH > 60%) leads to a minor increase in moisture content. A critical RH of approximately 74% was discovered, which is consistent with previous findings.[36,70] When the RH exceeds 74%, there is a drastic rise in moisture content (initially from 0.06% d.b. to 7.64% d.b. at 74% and ultimately to 326.5% d.b. at 95%).

A pronounced hysteresis loop is evident in Figure 2b, which illustrates an interplay between urea and water during the desorption cycle. It can be observed that the adsorption metastability starts at approximately 75% RH, concluding around 50% RH with each phase achieving equilibrium. To better understand this region, an analysis was conducted on the concentration of urea with its adsorbed water molecules across the full RH range. It was discerned that the urea concentration exceeds the critical dissolution threshold in a solution which is 20.14 mol/1000 g water at 25.5 °C[9] as shown in Figure 3a, showing a state of supersaturation for urea within this desorption RH level. At a RH level of 75%, the concentration was calculated to be approximately 20.21 M, greater than the critical concentration. This pattern of increase continued, culminating in a concentration of 46.2 M at a 50% RH. This allowed direct quantification of distinct phase regions that urea transitions through under equilibrium conditions, as shown in Figure 3b. In particular and based on the saturation concentration,[9] to reach a state of supersaturation, it necessitates 2.822 or fewer molecules of water per mole of urea. Moreover, the ratio of water molecules to urea moles was calculated to be around 2.748 at 75% RH, while it further declined to 1.202 at 50% RH.

Optical images as shown in Figure 3c were obtained over time of deliquescent urea at a steady state of 50% RH in the desorption cycle. Initial observations indicated that urea was entirely dissolved in the adsorbed water, representing a liquid state. As time advanced, it was noted that urea began to crystallize, a consequence of its supersaturated condition. This hysteresis loop is indicative of a robust affinity between urea and water molecules as, despite the metastability from 75 to 50% RH range, the interaction between water and urea molecules persisted in a manner that remained more favorable than the interaction between water molecules in the gas phase. This reveals a preference for water−urea bonds over water−water bonds under these conditions.

Modeling of Water Vapor Sorption Isotherms on Urea in the Monolayer and Multilayer Regime (RH < 60%). Numerous theories have been formulated to explain how sorbate (i.e., water vapor) interacts with sorbent (i.e., mineral dust particles) surfaces in conditions where the level of saturation is both below and above the normal limit. The Langmuir adsorption isotherm model has been recognized as the primary and most commonly applied model for adsorption among various models.[71] However, its use is restricted to adsorption occurring below a single layer. As a result, this model cannot effectively explain the adsorption of water on mineral dust particles in situations where high RH is involved.[46] Among other adsorption models, the Brunauer−Emmet−Teller (BET) equation (eq 2) is widely used to describe the adsorbate behavior and quantity on the surface of the adsorbent.[46,47] The BET model makes several adsorption-related assumptions, such as the gas molecules are monolayer-covered, the heat of adsorption of the first layer is unique, while the higher layers are equal to the energy of liquefication, and the Langmuir isotherm governs the adsorption process. These presumptions enable the formulation of a mathematical equation that can be applied to determine the material's surface area from the volume of gas adsorbed at various pressures.[48,72,73]

However, due to the limitations of BET fitting of water adsorption at RH > 50%,[44,45] many modifications attempted to enhance the applicability of BET. Anderson's[74] modification, for instance, enhanced both the physical interpretation and the fitting capabilities of the model. Anderson's equation was subsequently derived from a kinetic perspective by de Boer[75] and from a statistical standpoint by Guggenheim,[76] leading to the GAB equation (eq 3).

The GAB equation bears a resemblance to the BET equation; however, it incorporates an additional parameter (K) to account for the assumption that the sorption state of water molecules in all adsorption layers beyond the first is identical yet distinct from that in the pure liquid state. K adds an extra degree of freedom, which increases the versatility of the GAB model.[77,78] The parameter K denotes the discrepancy in the free enthalpy between water molecules in the pure liquid state and those in layers above the monolayer. When K assumes a value of 1, the GAB equation reduces to the BET equation.[77,78] It is

https://doi.org/10.1021/acsearthspacechem.3c00210
ACS Earth Space Chem. XXXX, XXX, XXX−XXX

noteworthy that the GAB model was applied to fit the water vapor isotherm on many amides.[79−81]

The BET, GAB, and Freundlich models were used to fit the experimental data shown in Figure 2a with the resulting fitting parameters and the fitting range and conditions compiled in Table 1. Figure 4a illustrates the effective fit of the Freundlich equation to the experimental data observed in the two linear regions; spanning from 5 to 20% RH with a coefficient of determination (R^2) valued at 0.985, and ranging from 25 to 60% RH with R^2 equating to 0.976. Beyond 65% RH, no linear regions were discernible, where the Freundlich equation could be applied, thereby indicating the constraints of this experimental model within the deliquescence region.

Table 1. Isotherm Models' Fitting Range and Parameters

model	fitting range	fitting parameters	statistical parameters
Freundlich	5% < RH < 20%	$k_f = 9.4 \times 10^{-5}$	$R^2 = 0.985$
		$n = 0.924$	
	25% < RH < 60%	$k_f = 1.17 \times 10^{-4}$	$R^2 = 0.976$
		$n = 0.982$	
BET	5% < RH < 50%	$W_m = 0.0423\%$	$R^2 = 0.83$
		$C_{BET} = 1.848$	
GAB	5% < RH < 74%	$K = 0.978$	$R^2 = 0.989$
		$W_m = 0.0278\%$	
		$C_{GAB} = 5.11$	

As presented in Figure 4b, the BET model shows a reasonable fitness to experimental data with an R^2 of ∼0.83, albeit its applicability is confined up to 50% (RH). In comparison, the GAB model demonstrates the best fitting capability, with an R^2 value of 0.989, extending its relevance to a higher RH of 74%. The monolayer formation according to BET is completed at 0.042% mass change, which is around 49.2% RH, while, according to GAB, the monolayer formation is found at 0.0278% mass change at 29.6% RH, which is more realistic and comparable to the literature data of 1.2 layer formation around 20% RH.[35] C_{BET} was determined to be less than 2, suggesting a type III isotherm and implying that the BET approach is not appropriate for modeling urea sorption behavior, as previously discussed in literature reports.[82] The fitting of GAB was only limited to 74% RH before deliquescence as trials to fit the model for higher RH lead to obtaining K values higher than 1, which is not physically consistent as the K range should be from 0 to 1.[49] However, C_{GAB} was higher than 2, which according to the literature indicates a type II isotherm which is not consistent with the observation in Figure 2b of urea sorption isotherm to be type III. Moreover, as mentioned in the literature, for $C_{GAB} \gg 1$ and $K \approx 1$, as in the case of urea isotherm, molecules forming multilayers are mainly behaving as in the bulk liquid state.[83] This finding corroborates the deliquescent behavior of urea, which can be attributed to the presence of water adsorbate layers exceeding the monolayer thickness, creating a liquid-like environment that facilitates urea dissolution.

As previously shown in the urea hygroscopic behavior, the sorption isotherm can be divided into three parts with the third section being the point at which deliquescence takes place. Consequently, the physical assumptions underlying the BET and GAB models are inadequate to account for the nature of the deliquescence process[68] at RH values exceeding 74%, resulting in significant discrepancies between the models and the observed data. These discrepancies initiated the need to look for different methods to describe the hygroscopic behavior of urea at a RH higher than the critical RH.

Modeling of Water Vapor Sorption Isotherms on Urea High RH Region (RH > 70%). A theoretical heat transport model in a prior study was developed by van Campen,[84] which provided a means of quantitatively predicting deliquescence kinetics, which is essential for understanding and predicting deliquescence behavior. Van Campen reported a series of articles that modeled and fitted experimental data of water uptake on deliquescent materials such as alkali halides and sugars at high RH.[84−86] First, a heat-transfer model was derived that calculates the water vapor uptake in an atmosphere of pure water vapor. Next, tests were performed on the models to validate the experimental data. Finally, in his third article, he described the same process as in article one, but in an inert atmosphere such as air.[84−86] The heat-transfer model shown in Figure 5a was developed based on some important assumptions and considerations such as the time spent in the nonsteady state is very short, and therefore, only the steady-state stage is considered in building the model, vapor diffusion can be ignored as the atmosphere is only pure water, and therefore, the heat flux and transport limit the rate of vapor condensation with the necessity of the heat transport to be released and transported to the surroundings. Furthermore, it was also assumed that the solid crystalline material's surface is surrounded by a saturated liquid film (see Figure 5b), which will maintain its saturation during steady-state uptake, and therefore, there is no

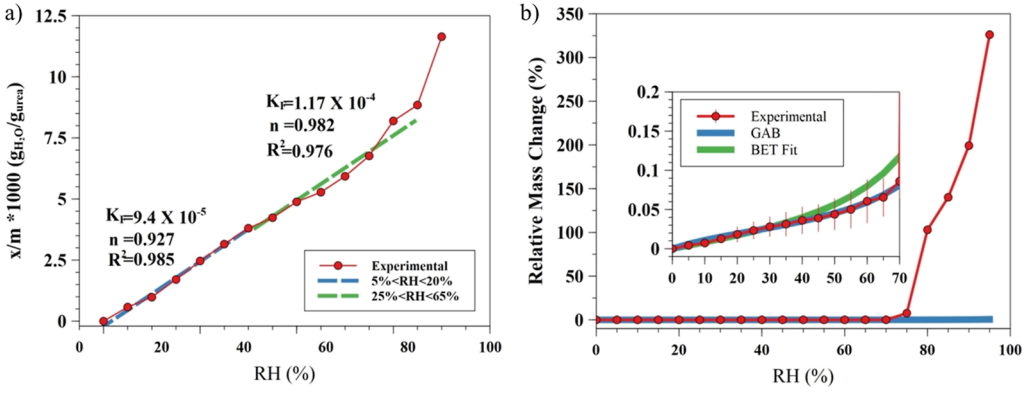

Figure 4. (a) Freundlich fit for water adsorption on urea in the two linear regions: 5−20% and 25−65% RH and (b) BET fit for water adsorption on urea until 50% and GAB fit until 70% RH.

https://doi.org/10.1021/acsearthspacechem.3c00210
ACS Earth Space Chem. XXXX, XXX, XXX−XXX

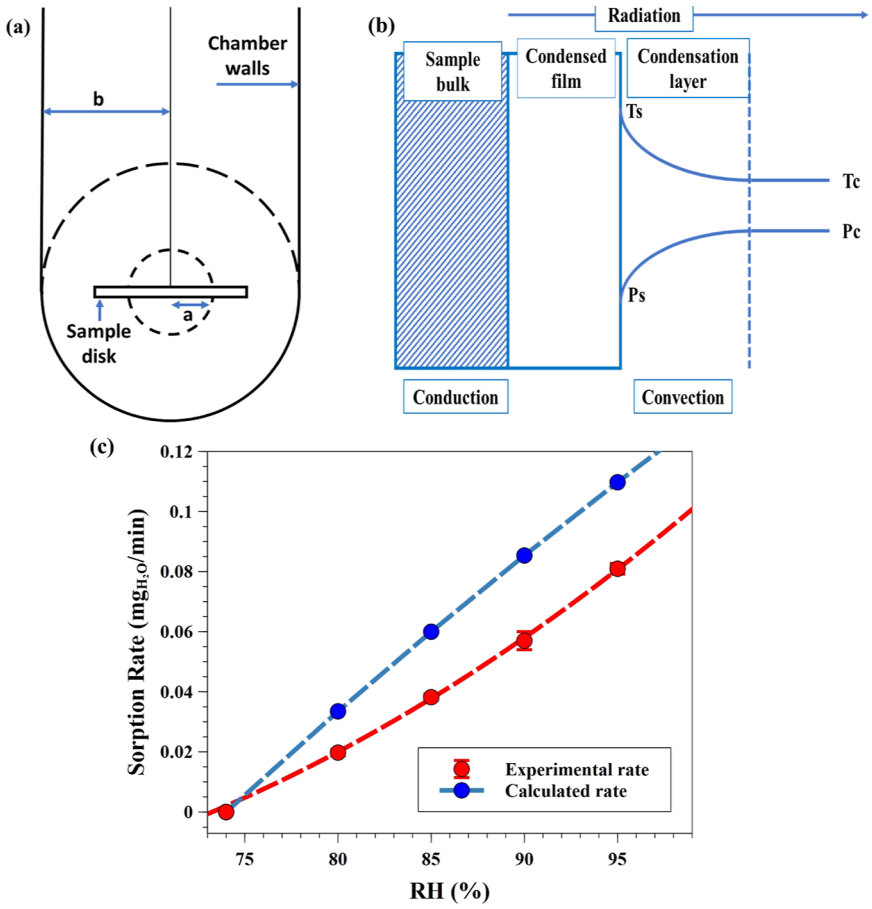

Figure 5. (a) Configuration of the heat-transfer model and (b) sample surface through deliquescence. Water−urea sorption data after deliquescence: (c) water sorption rate on urea after deliquescence as calculated using Van Campen's heat-transfer model and compared to experimentally acquired data.

Table 2. Pure Water Vapor Physical Parameters Used in the Transport Model Equation

parameter	value	unit	reference
a	0.23	cm	calculated values to maintain the surface area of the hypothetical hollow sphere to be equal to the actual disk surface area
b	10	cm	measured
M_w	18,000	mg/mol	Reference 82
ΔH	−9305	cal/mol	eq 10[85]
			C_{sat} = 20.14 mol/1000 g water[9]
			ΔH_{soln} = 3.67 kcal/mol[87]
ΔH_v	10,500	cal/mol	Reference 82
k	4.26×10^{-5}	cal/cm·sec·deg	
R	1.987	cal/K·mole	
T_c	298	K	
σ	1.36×10^{-12}	cal/cm^2·sec·deg^2	
e	0.95	°	

concentration gradient within the film. In addition, the sample disk is assumed to be presented as a hypothetical inner sphere of radius (a) for simplicity in deriving the model while maintaining the same surface area of the sample disk itself. The sample should be located symmetrically in a hemispherical base of a cylindrical chamber, which will be presented in the model as an outer sphere with a radius (b) as shown in Figure 5a.[84]

Based on these assumptions, the heat-transfer model describes the water vapor uptake rate as follows[84]

$$W = \left[\frac{60M_w \cdot 4\pi kab}{\Delta H(b-a)}\left(\frac{RT_c^2}{\Delta H_v - RT_c \ln \frac{RH_i}{RH_0}}\right) + \frac{60M_w \cdot 4\pi ka^2 \sigma e}{\Delta H}\left(\frac{4RT_c^5}{\Delta H_v - RT_c \ln \frac{RH_i}{RH_0}}\right)\right] \times \ln \frac{RH_i}{RH_0} \quad (9)$$

where W is the water sorption rate, M_w is the water molecular weight, a is the hypothetical sample radius, b is the chamber

https://doi.org/10.1021/acsearthspacechem.3c00210
ACS Earth Space Chem. XXXX, XXX, XXX−XXX

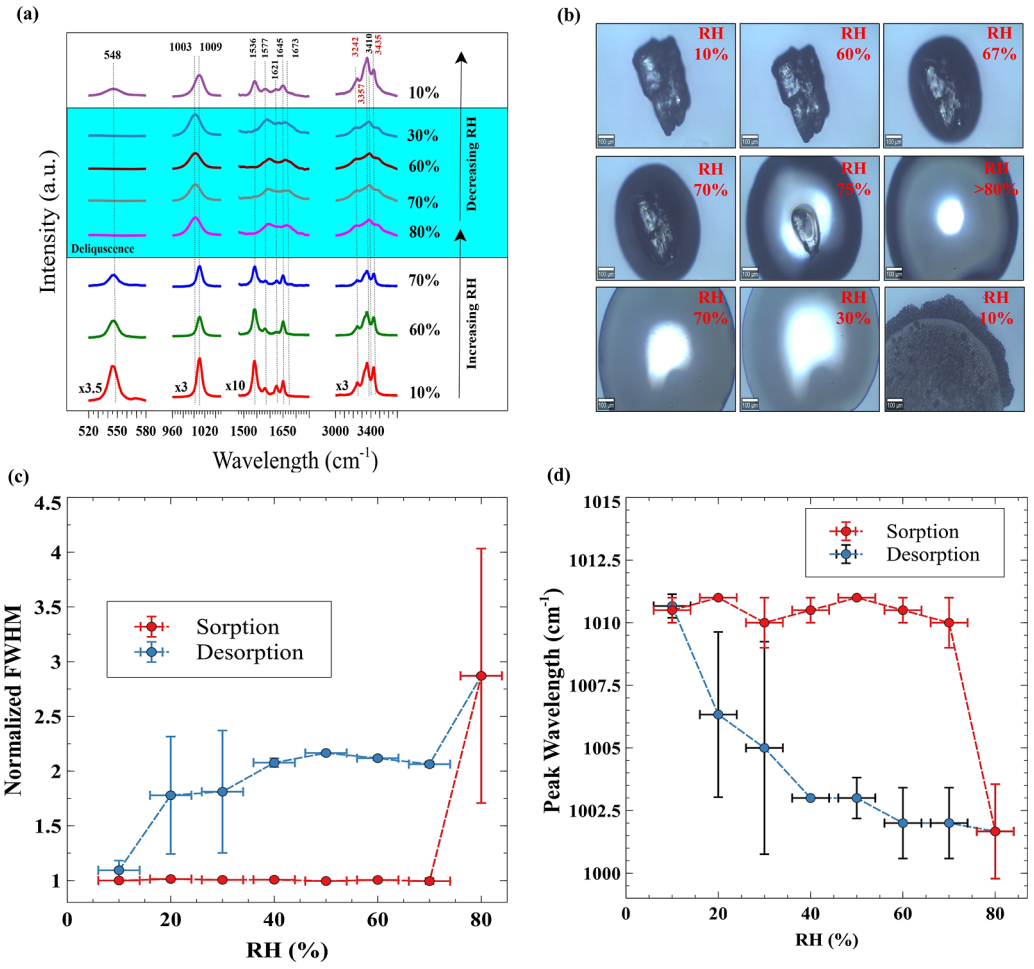

Figure 6. (a) In situ Raman spectrum of urea in different RH conditions, (b) in situ optical images of urea crystal under the corresponding RH conditions shown in (a), (c) normalized fwhm variations for the 1009 cm^{-1} peak with RH changes, and (d) peak shift of the same peak under the same RH conditions.

outer sphere radius, k is the thermal conductivity, R is the gas constant, T_c is the temperature of the chamber surface, RH_i is the RH of the atmosphere, RH_0 is the deliquescence RH, ΔH is the heat generated per unit of vapor condensed, ΔH_v is the heat of vaporization, σ is the Stefan–Boltzmann constant, and e is the radiation emissivity.[84] The first and second terms in the heat transport equation represent conduction and radiation processes, while convection was found to have a minor effect on the temperature gradient and therefore it was neglected.[84] The parameter values used to calculate the water vapor sorption rate are given in Table 2. The dimensions of the sample disk were measured so that the sample radius was 0.28 cm, while its height was 0.1 cm; hence, its surface area was calculated at ~0.67 cm^2, and consequently, the hypothetical a dimension was calculated to be 0.23 cm to ensure that the surface area of the hypothetical hollow sphere is equivalent to the actual disk's surface area. The chamber radius b was measured to be 10 cm. A procedure to calculate ΔH for solutions (eq 10) was demonstrated in the literature[85] using ΔH_c, which is water heat of condensation = −10.5 kcal/mol, ΔH_{soln} = 3.67 kcal/mol,[87] and saturation concentration, which is around 20.14 mol/L at 25.5 °C.[9] The remaining parameters used in eq 9 represent the physical constants that pertain to pure water.

$$\Delta H = -\Delta H_c + \frac{C_{sat}{}^{*}\Delta H_{soln}}{55.5} \quad (10)$$

Figure 5c shows the comparison between Van Campen's model and experimental results of the sorption rate at different RH % levels. At a 74% RH, the water sorption rate in both cases was found to be 0, meaning that there is no water sorption at the moment of deliquescence. As RH increases, the experimental water sorption rate shows a gradual rise, from 0.02 mg/min at 80% to 0.08 mg/min at 95%. Van Campen's model also exhibits an increasing trend, although the rates are slightly higher, ranging from 0.03 mg/min at 80% to 0.1 mg/min at 95%. The mean-square error (MAE) between the experimental and predicted data was 0.01 mg/min, showing a good agreement between the predicted and experimental values.

Single-Particle In Situ Raman Spectroscopy of Urea Interactions with Water Vapor. Under environmental conditions of RH, aerosols and fertilizer particles undergo abrupt and rapid fluctuations in humidity, failing to attain equilibrium promptly and causing their physical and chemical characteristics to undergo many changes.[88] Furthermore, the statistical generalization when analyzing bulk samples can sometimes lead to not accurately capturing the true nature of gas–particle interactions due to inherent compositional variations among individual particles.[89,90] Consequently, to investigate the different modifications in the crystal structure of urea induced by fluctuations in RH, an in situ analysis employing Raman spectroscopy was conducted on the urea particles. In particular, to facilitate clear monitoring of both the physical and

https://doi.org/10.1021/acsearthspacechem.3c00210
ACS Earth Space Chem. XXXX, XXX, XXX−XXX

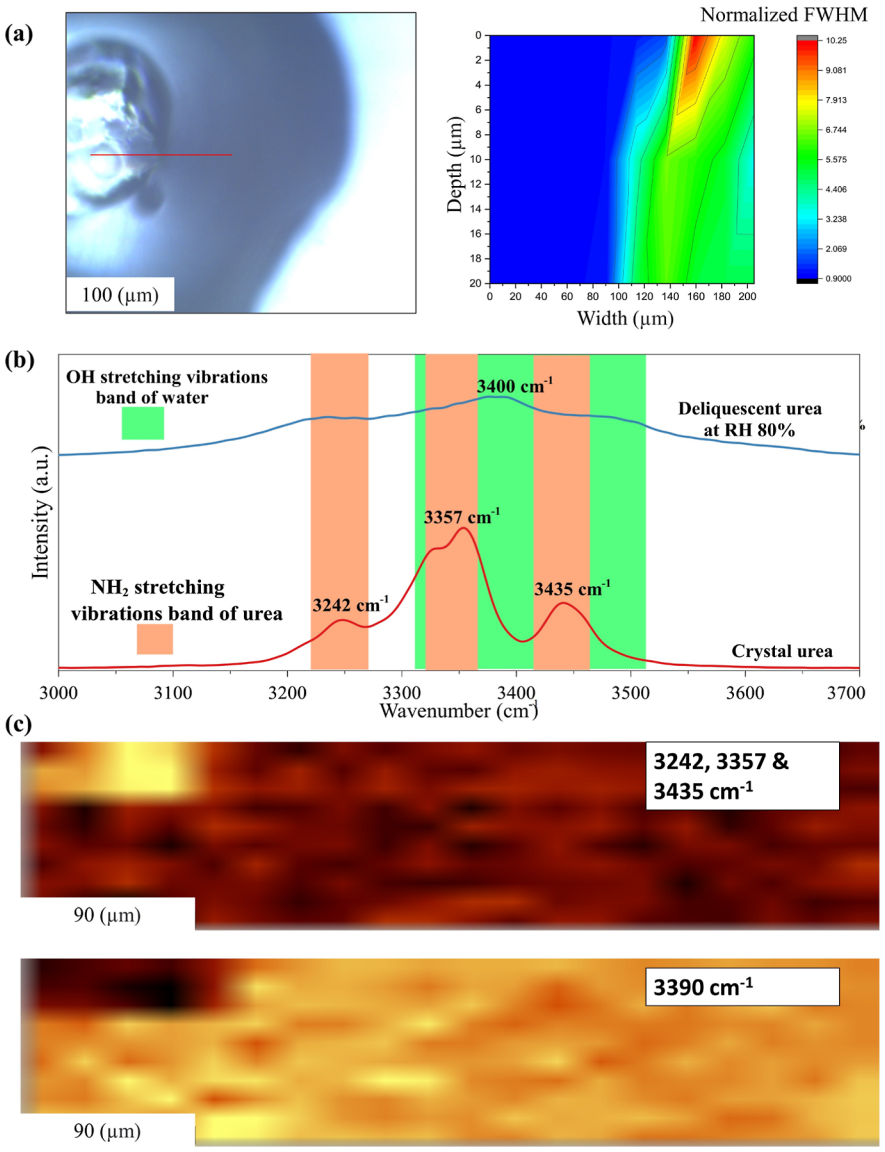

Figure 7. (a) Optical image of urea crystal at the initial stage of 80% RH showing its deliquescence and the area where the depth scan was performed and the corresponding normalized fwhm of 1009 cm^{-1} peak through the depth scan area, (b) in situ Raman spectrum comparison between crystalline urea under 10% RH and deliquescent urea, and (c) corresponding Raman depth scan mapping of NH_2 stretching vibration peaks and OH stretching vibration peaks under the same RH conditions as in (a) and (b).

chemical changes, and to comprehensively study the characteristic compositional peaks and interactions between molecules via shifts in peak positions and changes in peak widths, the single-particle analysis was conducted while systematically varying the RH conditions, ranging from 10 to 80%, and subsequently decreasing it from 80% back to 10%. The time between RH changes was 10 min to address the quick nonequilibrium changes due to urea−water interactions.

Upon inspection of the spectra for varying RH as depicted in Figure 6a, several noteworthy alterations in band frequencies were noticed.

Primarily, bands situated at 548 cm^{-1}, typically ascribed to the NCN bending mode,[91] and 1536 cm^{-1}, which corresponds to the NH_2 bending mode,[36,92] were observed at low RH. However, following the deliquescence of urea at RH > 70%, these bands became significantly more challenging to detect. Simultaneously, as deliquescence occurred and urea initiated the formation of more hydrogen bonds with water, the bands corresponding to the stretching modes of the free and hydrogen-bonded C−O group[92] at 1577 and 1645 cm^{-1} increased in intensity accompanied by the bands at 1621 and 1673 cm^{-1}. Additionally, the presence of the bands at 3435, 3357, and 3242 cm^{-1}, with a shoulder at 3323 cm^{-1}, which are typically linked to the antisymmetric and symmetric NH_2 stretching vibrations of urea,[91] was observed at low RH. These bands are then overlapped in deliquescent urea by the broadened peak representing the OH stretching mode[93] at 3410 cm^{-1}, attributable to the predominant water presence during this phase. Subsequently, as the system undergoes a desorption cycle leading to the elimination of all water content, these bands start to reappear strongly at 10% RH. Furthermore, the significant band observed at 1009 cm^{-1}, which is typically assigned to the NCN symmetric stretching mode,[94] underwent a minor broadening, and demonstrated a shift to a lower wavenumber at 1003 cm^{-1}. The evolution from a solid crystalline structure, transitioning into a liquid state upon deliquescence and

https://doi.org/10.1021/acsearthspacechem.3c00210
ACS Earth Space Chem. XXXX, XXX, XXX−XXX

ultimately concluding in recrystallization at lower RH values, is demonstrated in Figure 6b, which presents optical images elucidating the varying phases of a singular urea crystal under rapid and drastic alterations in RH. The significant alteration in the peak full width at half-maximum (fwhm) was utilized as a marker for phase transition,[90,95,96] while the observed shift in the peak's position might serve as an indicative signal of crystallization.[95] Typically, a substance in its liquid phase exhibits a broader fwhm compared to that of its solid phase. This is attributable to the less dense molecular configuration in the liquid phase, which permits minor discrepancies in vibrational characteristics.[90] Figure 6c illustrates the expansion of the band at 1009 cm^{-1} following the critical RH, as evidenced by the increase of the normalized fwhm from 1 to approximately 3. This widened state persists until all water molecules are eradicated at 10% RH, at which point the normalized fwhm reverts to its initial value. Also, a red shift of 1009 cm^{-1} band was noticed as shown in Figure 6d when deliquescence occurs at RH > 70% and it remained consistent until fully drying the crystal as the peak witnessed a blue shift to its initial value. A blue shift is consistent with the recrystallization of the sample as it has been reported in the literature with decreasing RH and water content.[97−99]

Subsequently, an investigation was undertaken to understand the behavior of the urea single crystal during its initial stage of deliquescence. This was achieved by performing a depth-resolved Raman scan in the initial phase when the RH reached 80%, before the crystal's complete transition into a liquid state. Figure 7 presents the optical image of the urea single crystal, distinctly combining both the solid and liquid phases, with the red line indicating the horizontal dimension of the acquired scan. The subsequent subsection of Figure 7a elucidates a computed map of 20 μm in depth by 200 μm in width, based on the 1009 cm^{-1} band normalized fwhm. This mapping effectively visualizes the distribution of the liquid and solid phases, represented by a gradation from heightened to decreased values, respectively. Building on and corroborating the previously illustrated Raman spectra, Figure 7b reveals the distinctive features of dissolved urea, characterized by the broadened OH vibration mode band at approximately 3400 cm^{-1}. Conversely, solid crystalline urea is denoted by its spectral bands at 3435, 3357, and 3242 cm^{-1}. Finally, Figure 7c depicts the depth maps of the broadened OH vibration band, highlighting the ensuing distribution of dissolved urea in its adsorbed water, and concurrently, the depth mapping of NH_2 stretching bands offers a comprehensive view of the distribution of crystalline urea.

Urea Single-Crystal Dissolution from Ab Initio Calculations from Monolayer to Bulk Water. Table 3 shows the resulting surface energies, in meV/A^2, of urea single-crystal surfaces under vacuum as well as those in the presence of a single monolayer and bulk water simulated as 55 M H_2O. Five different surface facets, including (001), (101), (110), (111), and (200), were selected as they represent the most stable facets determined experimentally and theoretically upon the growth of the crystals,[100,101] as shown in Figure 8. The resulting Wulff reconstructions are shown in Figure 9. While mainly (110) and (200) were determined to be prevalent under idealized vacuum conditions, the presence of 1 ML of water significantly changed the crystal shape of urea. In particular, the (111) facet became significant together with (101) and (110), while, in the presence of bulk H_2O, (101) became the dominant facet, notably, the extent to which this result can, in part, be affected by the particular structure of water in each surface slab model due to the multiple local minima where even modest changes in H-bonding can have significant consequences in surface energy calculations. Interestingly, the (101) facet has been shown to contribute little to the overall particle morphology but possessed higher binding energy toward H_2O molecules.[101] Thus, solvation of the urea crystal, as a first approximation as inferred from ab initio calculations, is predicted to be associated with the increased relative surface area of the (101) facet compared to other facets. Experimental observation in Figure 6b does not allow for the direct correlation between the experiment and theory since the as-received microcrystal growth conditions did not result in a well-defined crystal shape. However, data in Table 3 suggest that solvation results in the stabilization of higher order phases such as (111) and (101), which are normally of little relevance under idealistic vacuum conditions. Phenomenologically, single-crystal evolution shown in Figure 9 obtained using DFT calculations agrees with the single-particle imaging results in Figure 6b and suggests that high RH cycling changes the initial shape of the particle via new surface chemistry due to the interaction of urea and intercalated water molecules, as suggested by the appearance of new bands at 1673 cm^{-1} in the Raman spectrum that remain stable after desorption cycle and extended purging at 2% RH.

Table 3. PBE-D2 Calculated the Surface Energies of (001), (101), (110), (111), and (200) Urea Crystal Facets upon Varying Degrees of Solvation and the Corresponding Wulff Reconstructions

facet	γ_{vacuum}, meV/A^2	γ_{1MLH2O}, meV/A^2	$\gamma_{bulk\ H2O}$, meV/A^2
(001)	19.7	20.2	5.2
(101)	18.2	15.8	3.6
(110)	9.6	12.5	8.6
(111)	19.0	12.5	7.7
(200)	9.6	18.0	11.8

CONCLUSIONS

A detailed investigation of water as RH adsorption on urea particle surfaces was explored using a combination of DVS experiments, in situ single-particle Raman spectroscopy, and ab initio calculations. Raw DVS data showed three regimes of RH interactions with urea with 74% RH dramatically changing adsorbate−urea interaction behavior. The GAB model provided a superior description of the adsorption at <60% RH values, while a rigorously developed Van Campen model was used to fit the data acquired during the urea crystal deliquescence. The experimental water sorption rate showed a gradual rise from 0.02 mg/min at 80% to 0.08 mg/min at 95% in agreement with Van Campen's model of increasing trend, albeit at higher rates ranging from 0.03 mg/min at 80% to 0.1 mg/min at 95%. The MAE between the experimental and predicted data was 0.01 mg/min, showing a good agreement between the predicted and experimental values. In situ Raman spectroscopy combined with optical images of a single particle showed that the urea 1009 cm^{-1} peak fwhm can provide in-depth information about the transient phenomena taking place on the urea particle surface as well as in a partially liquefied environment. Finally, DFT results suggested Wulff's reconstruction of single urea crystals was dependent on the presence of the higher crystalline planes; particularly, the (111) facet became significant together with (101) and (110), while in the presence of bulk H_2O, (101) became the dominant facet. Overall, these results suggest that

https://doi.org/10.1021/acsearthspacechem.3c00210
ACS Earth Space Chem. XXXX, XXX, XXX−XXX

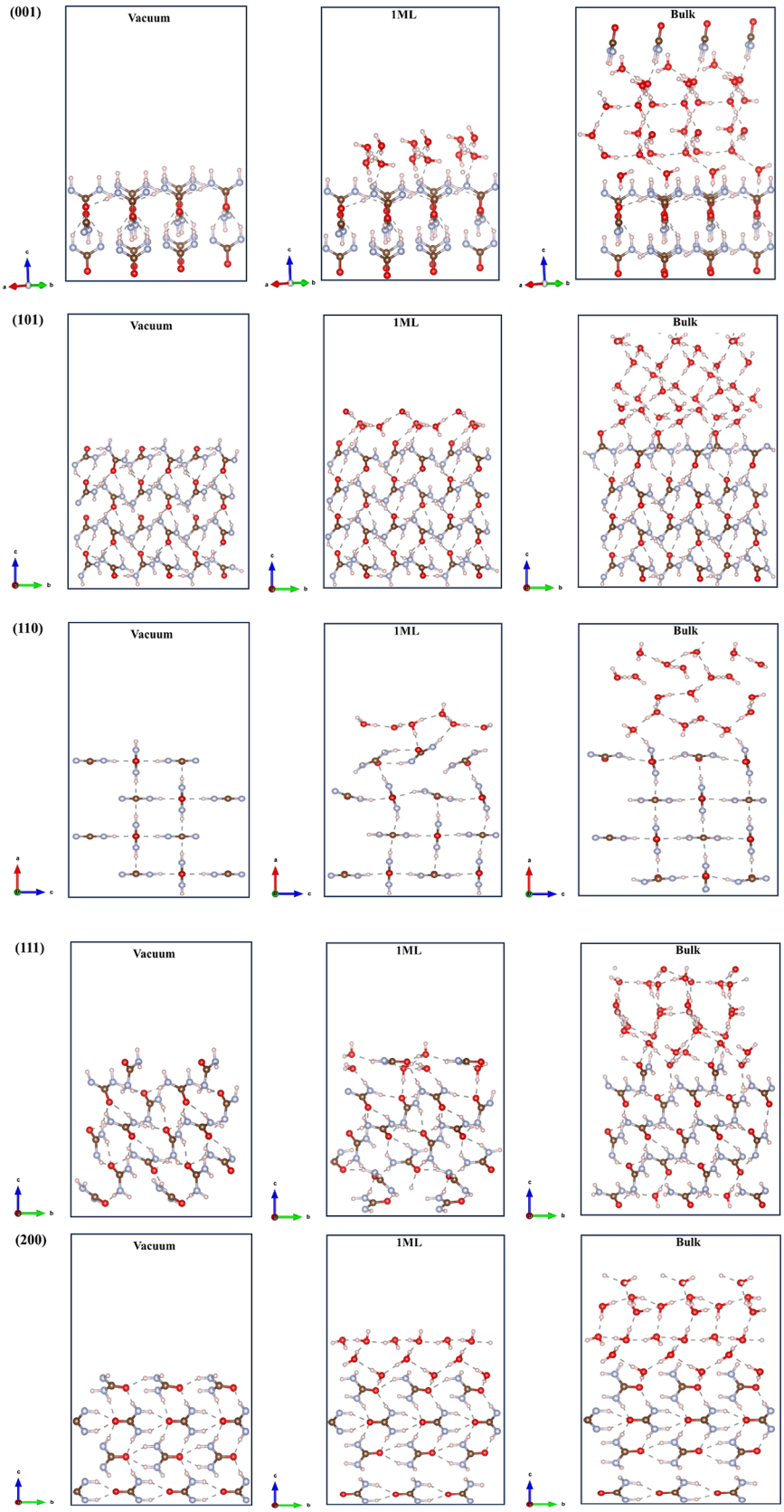

Figure 8. Lowest energy structures of the adsorbed water molecules on the predominant urea single-crystal facets (001), (101), (110), (111), and (200) terminated under vacuum in the presence of 1 ML as well as bulk H_2O.

particulate urea can undergo deliquescence in moist environments, those corresponding to high RH conditions, including both atmospheric and soil levels alike, and their environmental cycling will result in profound particle shape differences.

https://doi.org/10.1021/acsearthspacechem.3c00210
ACS Earth Space Chem. XXXX, XXX, XXX−XXX

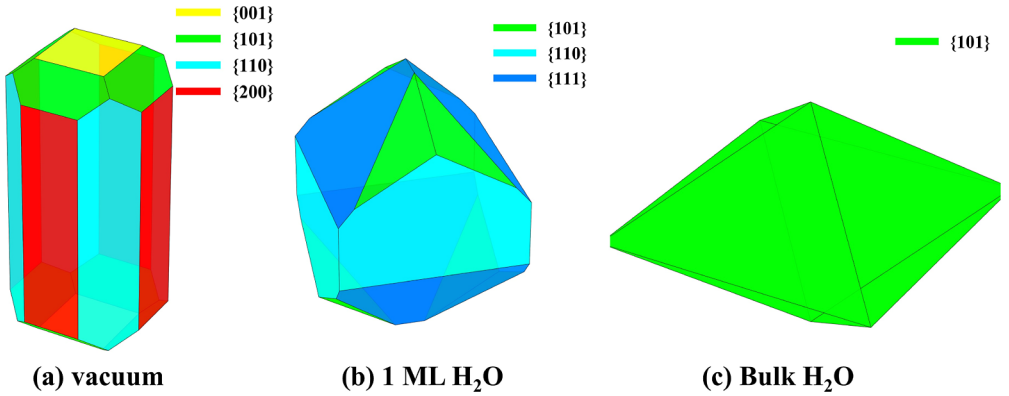

Figure 9. Wulff crystal reconstructions of urea crystals terminated under vacuum in the presence of 1 ML as well as bulk H_2O.

Concomitantly, this environmental cycling will stabilize new, potentially more reactive single particle facets which will be more prone toward interaction with soil moieties and undergo hydrolysis, especially in high pH soils, thus resulting in reactive nitrogen loss. The results outlined here also suggest that there is a need to actively explore soil component−urea interactions at the molecular, single-particle facet-dependent level under moist environments to better understand the resulting reactivity descriptors.

AUTHOR INFORMATION

Corresponding Author

Jonas Baltrusaitis − *Department of Chemical and Biomolecular Engineering, Lehigh University, Bethlehem, Pennsylvania 18015, United States;* orcid.org/0000-0001-5634-955X; Phone: +1-610-758-6836; Email: job314@lehigh.edu

Authors

Mohamed Eisa − *Department of Chemical and Biomolecular Engineering, Lehigh University, Bethlehem, Pennsylvania 18015, United States;* orcid.org/0000-0001-8821-2005

Dovilė Ragauskaitė − *Department of Chemical and Biomolecular Engineering, Lehigh University, Bethlehem, Pennsylvania 18015, United States*

Jingming Shi − *Department of Chemical and Biomolecular Engineering, Lehigh University, Bethlehem, Pennsylvania 18015, United States*

Seishi Shimizu − *York Structural Biology Laboratory, Department of Chemistry, University of York, YO10 5DD York, U.K.;* orcid.org/0000-0002-7853-1683

Tomas Bucko − *Department of Physical and Theoretical Chemistry, Faculty of Natural Sciences, Comenius University in Bratislava, 84215 Bratislava, Slovakia; Institute of Inorganic Chemistry, Slovak Academy of Sciences, 845 36 Bratislava, Slovakia;* orcid.org/0000-0002-5847-9478

Clinton Williams − *USDA-ARS, US Arid Land Agricultural Research Center, Maricopa, Arizona 85138, United States*

Complete contact information is available at: https://pubs.acs.org/10.1021/acsearthspacechem.3c00210

Funding

This work was supported by the Engineering for Agricultural Production Systems program grant no. 2020-67022-31144 from the USDA National Institute of Food and Agriculture. This research used resources provided by the SCINet project of the USDA Agricultural Research Service, ARS project number 0500-00093-001-00-D.

Notes

The authors declare no competing financial interest.

REFERENCES

(1) Comer, B. M.; Fuentes, P.; Dimkpa, C. O.; Liu, Y. H.; Fernandez, C. A.; Arora, P.; Realff, M.; Singh, U.; Hatzell, M. C.; Medford, A. J. Prospects and Challenges for Solar Fertilizers. *Joule* **2019**, *3* (7), 1578−1605.

(2) Zhu, X.; Zhou, X.; Jing, Y.; Li, Y. Electrochemical Synthesis of Urea on MBenes. *Nat. Commun.* **2021**, *12* (1), 4080−4089.

(3) Smil, V. *Enriching the Earth: Fritz Haber, Carl Bosch, and the Transformation of World Food Production*; MIT Press, 2004.

(4) Eisa, M.; Ragauskaitė, D.; Adhikari, S.; Bella, F.; Baltrusaitis, J. Role and Responsibility of Sustainable Chemistry and Engineering in Providing Safe and Sufficient Nitrogen Fertilizer Supply at Turbulent Times. *ACS Sustain. Chem. Eng.* **2022**, *10* (28), 8997−9001.

(5) Vaughan, P.; Donohue, J. The Structure of Urea. Interatomic Distances and Resonance in Urea and Related Compounds. *Acta Crystallogr.* **1952**, *5* (4), 530−535.

(6) Zavodnik, V.; Stash, A.; Tsirelson, V.; De Vries, R.; Feil, D. Electron Density Study of Urea Using TDS-Corrected X-Ray Diffraction Data: Quantitative Comparison of Experimental and Theoretical Results. *Acta Crystallogr.* **1999**, *55*, 45−54.

(7) Roseman, M.; Jencks, W. P. Interactions of Urea and Other Polar Compounds in Water. *J. Am. Chem. Soc.* **1975**, *97*, 631−640.

(8) Pinck, L. A.; Kelly, M. A. The Solubility of Urea in Water. *J. Am. Chem. Soc.* **1925**, *47* (8), 2170−2172.

(9) Lee, F. M.; Lahti, L. E. Solubility of Urea in Water-Alcohol Mixtures. *J. Chem. Eng. Data* **1972**, *17* (3), 304−306.

(10) Marepula, H.; Courtney, C. E.; Randall, D. G. Urea Recovery from Stabilized Urine Using a Novel Ethanol Evaporation and Recrystallization Process. *Chem. Eng. J. Adv.* **2021**, *8*, 100174.

(11) Han, S.; Hong, J.; Luo, Q.; Xu, H.; Tan, H.; Wang, Q.; Tao, J.; Zhou, Y.; Peng, L.; He, Y.; Shi, J.; Ma, N.; Cheng, Y.; Su, H. Hygroscopicity of Organic Compounds as a Function of Organic Functionality, Water Solubility, Molecular Weight, and Oxidation Level. *Atmos. Chem. Phys.* **2022**, *22*, 3985−4004.

(12) Mauer, L. J. Deliquescence of Crystalline Materials: Mechanism and Implications for Foods. *Curr. Opin. Food Sci.* **2022**, *46*, 100865.

(13) Adams, J. R.; Merz, A. R. Hygroscopicity of Fertilizer Materials and Mixtures. *Ind. Eng. Chem.* **1929**, *21* (4), 305−307.

(14) Thakral, S. Study of Moisture Sorption Behavior of Urea Inclusion Compounds with Aliphatic Guests and with Linear Polymers. *J. Phys. Org. Chem.* **2014**, *27*, 76−86.

(15) Werner, E. Urea as a Hygroscopic Substance. *Nature* **1937**, *139*, 512.

(16) Ernst, J. W.; Massey, H. F. The Effects of Several Factors on Volatilization of Ammonia Formed from Urea in the Soil. *Soil Sci. Soc. Am. J.* **1960**, *24* (2), 87−90.

(17) Milchunas, D. G.; Parton, W. J.; Bigelow, D. S.; Schimel, D. S. Factors Influencing Ammonia Volatilization from Urea in Soils of the Shortgrass Steppe. *J. Atmos. Chem.* **1988**, *6* (4), 323−340.
(18) Sommer, S. G.; Jensen, C. Ammonia Volatilization from Urea and Ammoniacal Fertilizers Surface Applied to Winter Wheat and Grassland. *Fertil. Res.* **1994**, *37*, 85−92.
(19) Black, A. S.; Sherlock, R. R.; Smith, N. P. Effect of Timing of Simulated Rainfall on Ammonia Volatilization from Urea, Applied to Soil of Varyingmoisture Content. *J. Soil Sci.* **1987**, *38* (4), 679−687.
(20) Ferguson, R. B.; Kissel, D. E. Effects of Soil Drying on Ammonia Volatilization from Surface-applied Urea. *Soil Sci. Soc. Am. J.* **1986**, *50* (2), 485−490.
(21) Titko, S.; Street, J. R.; Logan, T. J. Volatilization of Ammonia from Granular and Dissolved Urea Applied to Turfgrass. *Agron. J.* **1987**, *79* (3), 535−540.
(22) Bouwmeester, R. J. B.; Vlek, P. L. G.; Stumpe, J. M. Effect of Environmental Factors on Ammonia Volatilization from a Urea-Fertilized Soil. *Soil Sci. Soc. Am. J.* **1985**, *49* (2), 376−381.
(23) Cabrera, M. L.; Kissel, D. E.; Craig, J. R.; Qafoku, N. P.; Vaio, N.; Rema, J. A.; Morris, L. A. Relative Humidity Controls Ammonia Loss from Urea Applied to Loblolly Pine. *Soil Sci. Soc. Am. J.* **2010**, *74* (2), 543−549.
(24) Kiss, S.; Simihăian, M. *Improving Efficiency of Urea Fertilizers by Inhibition of Soil Urease Activity*; Springer Netherlands: Dordrecht, 2002.
(25) Brondi, M.; Eisa, M.; Bortoletto-Santos, R.; Drapanauskaite, D.; Reddington, T.; Williams, C.; Ribeiro, C.; Baltrusaitis, J. Recovering, Stabilizing, and Reusing Nitrogen and Carbon from Nutrient-Containing Liquid Waste as Ammonium Carbonate Fertilizer. *Agric.* **2023**, *13* (4), 909.
(26) Anas, M.; Liao, F.; Verma, K. K.; Sarwar, M. A.; Mahmood, A.; Chen, Z.-L.; Li, Q.; Zeng, X.-P.; Liu, Y.; Li, Y.-R. Fate of Nitrogen in Agriculture and Environment: Agronomic, Eco-Physiological and Molecular Approaches to Improve Nitrogen Use Efficiency. *Biol. Res.* **2020**, *53* (1), 47.
(27) Giordano, M.; Petropoulos, S. A.; Rouphael, Y. The Fate of Nitrogen from Soil to Plants: Influence of Agricultural Practices in Modern Agriculture. *Agric.* **2021**, *11* (10), 944.
(28) Erisman, J. W.; Galloway, J.; Seitzinger, S.; Bleeker, A.; Butterbach-Bahl, K. Reactive Nitrogen in the Environment and Its Effect on Climate Change. *Curr. Opin. Environ. Sustain.* **2011**, *3* (5), 281−290.
(29) Bista, P.; Eisa, M.; Ragauskaite, D.; Sapkota, S.; Baltrusaitis, J.; Ghimire, R. Effect of Urea-Calcium Sulfate Cocrystal Nitrogen Fertilizer on Sorghum Productivity and Soil N2O Emissions. *Sustainability* **2023**, *15* (10), 8010.
(30) Patil, B. S.; Wang, Q.; Hessel, V.; Lang, J. Plasma N2-Fixation: 1900−2014. *Catal. Today* **2015**, *256*, 49−66.
(31) Cornell, S. E.; Jickells, T. D.; Thornton, C. A. Urea in Rainwater and Atmospheric Aerosol. *Atmos. Environ.* **1998**, *32* (11), 1903−1910.
(32) Mace, K. A.; Duce, R. A.; Tindale, N. W. Organic Nitrogen in Rain and Aerosol at Cape Grim, Tasmania, Australia. *J. Geophys. Res., C: Oceans Atmos.* **2003**, *108* (D11), 4338.
(33) Matsumoto, K.; Yamamoto, Y.; Kim, S.; Irino, T.; Yoshikawa-Inoue, H. Chemical Characterization of the Water-Soluble Organic Nitrogen in the Maritime Aerosol. *J. Aerosol Sci.* **2023**, *167* (July 2022), 106069.
(34) Matsumoto, K.; Yamamoto, Y.; Kobayashi, H.; Kaneyasu, N.; Nakano, T. Water-Soluble Organic Nitrogen in the Ambient Aerosols and Its Contribution to the Dry Deposition of Fixed Nitrogen Species in Japan. *Atmos. Environ.* **2014**, *95*, 334−343.
(35) Kanazawa, T.; Chikazawa, M.; Kaiho, M.; Kikuchi, M. The Relationship between Caking and Changes in Surface Properties of Urea Particles Due to Moisture Absorption. *J. Res. Assoc. Powder Technol., Jpn.* **1976**, *13* (8), 411−416.
(36) Silva, M.; Barcauskaite, K.; Drapanauskaite, D.; Tian, H.; Bučko, T.; Baltrusaitis, J. Relative Humidity Facilitated Urea Particle Reaction with Salicylic Acid: A Combined in Situ Spectroscopy and DFT Study. *ACS Earth Space Chem.* **2020**, *4* (7), 1018−1028.
(37) Clegg, S. L.; Brimblecombe, P.; Wexler, A. S. Thermodynamic Model of the System H+-NH4+-SO42-NO 3-H2O at Tropospheric Temperatures. *J. Phys. Chem. A* **1998**, *102* (12), 2137−2154.
(38) Fountoukis, C.; Nenes, A. ISORROPIAII: A Computationally Efficient Thermodynamic Equilibrium Model for K+-Ca2+-Mg2+-NH4+-Na+-SO42-NO3-Cl-H2O Aerosols. *Atmos. Chem. Phys.* **2007**, *7* (17), 4639−4659.
(39) Hanford, K. L.; Mitchem, L.; Reid, J. P.; Clegg, S. L.; Topping, D. O.; McFiggans, G. B. Comparative Thermodynamic Studies of Aqueous Glutaric Acid, Ammonium Sulfate and Sodium Chloride Aerosol at High Humidity. *J. Phys. Chem. A* **2008**, *112* (39), 9413−9422.
(40) Wu, L.; Li, X.; Ro, C. U. Hygroscopic Behavior of Ammonium Sulfate, Ammonium Nitrate, and Their Mixture Particles. *Asian J. Atmos. Environ.* **2019**, *13* (3), 196−211.
(41) Mazzei, L.; Broll, V.; Casali, L.; Silva, M.; Braga, D.; Grepioni, F.; Baltrusaitis, J.; Ciurli, S. Multifunctional Urea Cocrystal with Combined Ureolysis and Nitrification Inhibiting Capabilities for Enhanced Nitrogen Management. *ACS Sustain. Chem. Eng.* **2019**, *7* (15), 13369−13378.
(42) Subramanyam, B.; Das, A. Linearised and Non-Linearised Isotherm Models Optimization Analysis by Error Functions and Statistical Means. *J. Environ. Health Sci. Eng.* **2014**, *12* (1), 92.
(43) Hatch, C. D. C. D.; Wiese, J. S. J. S.; Crane, C. C. C. C.; Harris, K. J. K. J.; Kloss, H. G. H. G.; Baltrusaitis, J. Water Adsorption on Clay Minerals As a Function of Relative Humidity: Application of BET and Freundlich Adsorption Models. *Langmuir* **2012**, *28* (3), 1790−1803.
(44) Lewicki, P. P. The Applicability of the GAB Model to Food Water Sorption Isotherms. *Int. J. Food Sci. Technol.* **1997**, *32* (6), 553−557.
(45) Timmermann, E. O.; Chirife, J.; Iglesias, H. A. Water Sorption Isotherms of Foods and Foodstuffs: BET or GAB Parameters? *J. Food Eng.* **2001**, *48* (1), 19−31.
(46) Tang, M.; Cziczo, D. J.; Grassian, V. H. Interactions of Water with Mineral Dust Aerosol: Water Adsorption, Hygroscopicity, Cloud Condensation, and Ice Nucleation. *Chem. Rev.* **2016**, *116* (7), 4205−4259.
(47) Silva, M.; Eisa, M.; Ragauskaitė, D.; Baltrusaitis, J. Water Sorption on Formic Acid-Modified Hydroxyapatite as a Function of Relative Humidity: Simulated Environmental Aging Effects on Hygroscopicity and Nutrient Release. *ACS Earth Space Chem.* **2022**, *6*, 3043−3053.
(48) Van Erp, T. S.; Martens, J. A. A Standardization for BET Fitting of Adsorption Isotherms. *Microporous Mesoporous Mater.* **2011**, *145* (1−3), 188−193.
(49) Blahovec, J.; Yanniotis, S. Gab Generalized Equation for Sorption Phenomena. *Food Bioprocess Technol.* **2008**, *1* (1), 82−90.
(50) Schär, W.; Rüegg, M. The Evaluation of GAB Constants from Water Vapour Sorption Data. *Lebensm Wiss Technol.* **1985**, *18*, 225−229.
(51) Kresse, G.; Hafner, J. Ab Initio Molecular-Dynamics Simulation of the Liquid-Metal-Amorphous-Semiconductor Transition in Germanium. *Phys. Rev. B: Condens. Matter Mater. Phys.* **1994**, *49* (20), 14251−14269.
(52) Kresse, G.; Furthmüller, J. Efficiency of Ab-Initio Total Energy Calculations for Metals and Semiconductors Using a Plane-Wave Basis Set. *Comput. Mater. Sci.* **1996**, *6* (1), 15−50.
(53) Kresse, G.; Furthmüller, J. Efficient Iterative Schemes for Ab Initio Total-Energy Calculations Using a Plane-Wave Basis Set. *Phys. Rev. B: Condens. Matter Mater. Phys.* **1996**, *54* (16), 11169−11186.
(54) Kresse, G.; Hafner, J. Ab Initio Molecular Dynamics for Open-Shell Transition Metals. *Phys. Rev. B: Condens. Matter Mater. Phys.* **1993**, *48* (17), 13115−13118.
(55) Blöchl, P. E. Projector Augmented-Wave Method. *Phys. Rev. B: Condens. Matter Mater. Phys.* **1994**, *50* (24), 17953−17979.
(56) Kresse, G.; Joubert, D. From Ultrasoft Pseudopotentials to the Projector Augmented-Wave Method. *Phys. Rev. B: Condens. Matter Mater. Phys.* **1999**, *59* (3), 1758−1775.

https://doi.org/10.1021/acsearthspacechem.3c00210
ACS Earth Space Chem. XXXX, XXX, XXX−XXX

(57) Perdew, J. P.; Burke, K.; Ernzerhof, M. Generalized Gradient Approximation Made Simple. *Phys. Rev. Lett.* **1996**, *77* (18), 3865−3868.
(58) Bučko, T.; Hafner, J.; Lebègue, S.; Ángyán, J. G. Improved Description of the Structure of Molecular and Layered Crystals: Ab Initio DFT Calculations with van Der Waals Corrections. *J. Phys. Chem. A* **2010**, *114* (43), 11814−11824.
(59) Grimme, S. Semiempirical GGA-Type Density Functional Constructed with a Long-Range Dispersion Correction. *J. Comput. Chem.* **2006**, *27* (15), 1787−1799.
(60) Guth, H.; Heger, G.; Klein, S.; Treutmann, W.; Scheringer, C. Strukturverfeinerung von Harnstoff Mit Neutronenbeugungsdaten Bei 60, 123 Und 293 K Und X-N- Und X-X(1s2)-Synthesen Bei Etwa 100 K. *Z. Kristallogr.—Cryst. Mater.* **1980**, *153* (1−4), 237−254.
(61) Murnaghan, F. D. The Compressibility of Media under Extreme Pressures. *Proc. Natl. Acad. Sci. U.S.A.* **1944**, *30* (9), 244−247.
(62) Andersen, H. C. Molecular Dynamics Simulations at Constant Pressure and/or Temperature. *J. Chem. Phys.* **1980**, *72* (4), 2384−2393.
(63) Wulff, G. XXV. Zur Frage der Geschwindigkeit des Wachsthums und der Auflösung der Krystallflächen. *Z. Kristallogr.—Cryst. Mater.* **1901**, *34* (1−6), 449−530.
(64) Rahm, J.; Erhart, P. WulffPack: A Python Package for Wulff Constructions. *J. Open Source Softw.* **2020**, *5* (45), 1944.
(65) Brunauer, S.; Deming, L. S.; Deming, W. E.; Teller, E. On a Theory of the van Der Waals Adsorption of Gases. *J. Am. Chem. Soc.* **1940**, *62* (7), 1723−1732.
(66) Silva, M.; Baltrus, J. P.; Burnett, D. J.; Baltrusaitis, J. Water Adsorption on Hydroxyapatite and Struvite as a Function of Relative Humidity: Application of BET and Freundlich Adsorption Models. *ACS Earth Space Chem.* **2022**, *6* (2), 431−443.
(67) Andrade P, R. D.; Lemus M, R.; Pérez C, C. E. C. E. Models of Sorption Isotherms for Food: Uses and Limitations. *Vitae* **2011**, *18* (3), 325−334.
(68) Shimizu, S.; Matubayasi, N. Sorption: A Statistical Thermodynamic Fluctuation Theory. *Langmuir* **2021**, *37* (24), 7380−7391.
(69) Phahom, T.; Roudaut, G. Moisture Sorption Characteristics and Dynamic Mechanical Thermal Analysis of Dried Petiole and Rhizome of Red Water Lily (Nymphaea x Rubra). *Heat Mass Transfer* **2023**, *59* (2), 309−328.
(70) Casali, L.; Mazzei, L.; Shemchuk, O.; Sharma, L.; Honer, K.; Grepioni, F.; Ciurli, S.; Braga, D.; Baltrusaitis, J. Novel Dual-Action Plant Fertilizer and Urease Inhibitor: Urea·Catechol Cocrystal. Characterization and Environmental Reactivity. *ACS Sustain. Chem. Eng.* **2019**, *7* (2), 2852−2859.
(71) Lowell, S.; Shields, J. E.; Thomas, M. A.; Thommes, M. *Characterization of Porous Solids and Powders: Surface Area, Pore Size and Density*; Springer: Amsterdam, the Netherlands, 2004.
(72) McMillan, W. G.; Teller, E. The Assumptions of the B.E.T. Theory. *J. Phys. Chem.* **1951**, *55* (1), 17−20.
(73) Langmuir, I. The Constitution and Fundamental Properties of Solids and Liquids. *J. Am. Chem. Soc.* **1916**, *38*, 2221−2295.
(74) Anderson, R. B. Modifications of the Brunauer, Emmett and Teller Equation. *J. Am. Chem. Soc.* **1946**, *68* (4), 686−691.
(75) de Boer, J. H. *The Dynamical Character of Adsorption*; Oxford University Press: London, 1953.
(76) Guggenheim, E. A. *Applications of Statistical Mechanics*; Oxford University Press: London, 1966.
(77) Timmermann, E. O. A B.E.T.-like Three Sorption Stage Isotherm. *J. Chem. Soc., Faraday Trans. 1* **1989**, *85* (7), 1631−1645.
(78) Arthur, E.; Tuller, M.; Moldrup, P.; Greve, M. H.; Knadel, M.; de Jonge, L. W. Applicability of the Guggenheim-Anderson-Boer Water Vapour Sorption Model for Estimation of Soil Specific Surface Area. *Eur. J. Soil Sci.* **2018**, *69* (2), 245−255.
(79) Lim, L. T.; Britt, I. J.; Tung, M. A. Sorption and Transport of Water Vapor in Nylon 6,6 Film. *J. Appl. Polym. Sci.* **1999**, *71* (2), 197−206.
(80) Jonquières, A.; Fane, A. Modified BET Models for Modeling Water Vapor Sorption in Hydrophilic Glassy Polymers and Systems Deviating Strongly from Ideality. *J. Appl. Polym. Sci.* **1998**, *67* (8), 1415−1430.
(81) Mucha, M.; Wańkowicz, K.; Balcerzak, J. Analysis of Water Adsorption on Chitosan and Its Blends with Hydroxypropylcellulose. *e-Polym.* **2007**, *7* (016), 1−10.
(82) Thommes, M.; Kaneko, K.; Neimark, A. V.; Olivier, J. P.; Rodriguez-Reinoso, F.; Rouquerol, J.; Sing, K. S. W. Physisorption of Gases, with Special Reference to the Evaluation of Surface Area and Pore Size Distribution (IUPAC Technical Report). *Pure Appl. Chem.* **2015**, *87* (9−10), 1051−1069.
(83) Quirijns, E. J.; Van Boxtel, A. J. B.; Van Loon, W. K. P.; Van Straten, G. Sorption Isotherms, GAB Parameters and Isosteric Heat of Sorption. *J. Sci. Food Agric.* **2005**, *85* (11), 1805−1814.
(84) van Campen, L.; Amidon, G. L.; Zografi, G. Moisture Sorption Kinetics for Water-soluble Substances I: Theoretical Considerations of Heat Transport Control. *J. Pharm. Sci.* **1983**, *72* (12), 1381−1388.
(85) van Campen, L.; Amidon, G. L.; Zografi, G. Moisture Sorption Kinetics for Water-soluble Substances II: Experimental Verification of Heat Transport Control. *J. Pharm. Sci.* **1983**, *72* (12), 1388−1393.
(86) van Campen, L.; Amidon, G. L.; Zografi, G. Moisture Sorption Kinetics for Water-soluble Substances III: Theoretical and Experimental Studies in Air. *J. Pharm. Sci.* **1983**, *72* (12), 1394−1398.
(87) Taniewska-Osińska, S.; Piestrzyńska, B.; Łogwinienko, R. The Enthalpy of Solution of NaI, NaCl, NaClO4, and Urea in Water-Tetrahydrofuran Mixtures at 298.15 K. *Can. J. Chem.* **1980**, *58* (15), 1584−1588.
(88) Eastwood, P. Formation II: Location. *Particulate Emissions from Vehicles*; Wiley, 2008; pp 135−155, Chapter 4.
(89) Ault, A. P.; Axson, J. L. Atmospheric Aerosol Chemistry: Spectroscopic and Microscopic Advances. *Anal. Chem.* **2017**, *89* (1), 430−452.
(90) Liang, Z.; Chu, Y.; Gen, M.; Chan, C. K. Single-Particle Raman Spectroscopy for Studying Physical and Chemical Processes of Atmospheric Particles. *Atmos. Chem. Phys.* **2022**, *22* (5), 3017−3044.
(91) Frost, R. L.; Kristof, J.; Rintoul, L.; Kloprogge, J. T. Raman Spectroscopy of Urea and Urea-Intercalated Kaolinites at 77 K. *Spectrochim. Acta, Part A* **2000**, *56* (9), 1681−1691.
(92) Acosta-Maeda, T. E.; Misra, A. K.; Muzangwa, L. G.; Berlanga, G.; Muchow, D.; Porter, J.; Sharma, S. K. Remote Raman Measurements of Minerals, Organics, and Inorganics at 430 m Range. *Appl. Opt.* **2016**, *55* (36), 10283.
(93) Wang, Z.; Pakoulev, A.; Pang, Y.; Dlott, D. D. Vibrational Substructure in the OH Stretching Transition of Water and HOD. *J. Phys. Chem. A* **2004**, *108* (42), 9054−9063.
(94) Keuleers, R.; Desseyn, H. O.; Rousseau, B.; Van Alsenoy, C. Vibrational Analysis of Urea. *J. Phys. Chem. A* **1999**, *103* (24), 4621−4630.
(95) Chan, L. P.; Chan, C. K. Roles of the Phase State and Water Content in Ozonolysis of Internal Mixtures of Maleic Acid and Ammonium Sulfate Particles. *Aerosol Sci. Technol.* **2012**, *46* (7), 781−793.
(96) Ling, T. Y.; Chan, C. K. Partial Crystallization and Deliquescence of Particles Containing Ammonium Sulfate and Dicarboxylic Acids. *J. Geophys. Res.: Atmos.* **2008**, *113* (D14), D14205.
(97) Lee, A. K. Y.; Ling, T. Y.; Chan, C. K. Understanding Hygroscopic Growth and Phase Transformation of Aerosols Using Single Particle Raman Spectroscopy in an Electrodynamic Balance. *Faraday Discuss.* **2008**, *137* (852), 245−263.
(98) Li, X. H.; Wang, F.; Lu, P. D.; Dong, J. L.; Wang, L. Y.; Zhang, Y. H. Confocal Raman Observation of the Efflorescence/Deliquescence Processes of Individual NaNO3 Particles on Quartz. *J. Phys. Chem. B* **2006**, *110* (49), 24993−24998.
(99) Wang, L. Y.; Zhang, Y. H.; Zhao, L. J. Raman Spectroscopic Studies on Single Supersaturated Droplets of Sodium and Magnesium Acetate. *J. Phys. Chem. A* **2005**, *109* (4), 609−614.
(100) George, A. R.; Harris, K. D. M.; Rohl, A. L.; Gay, D. H. Computational Investigation of Surface Structural Relaxation in Crystalline Urea. *J. Mater. Chem.* **1995**, *5* (1), 133−139.

https://doi.org/10.1021/acsearthspacechem.3c00210
ACS Earth Space Chem. XXXX, XXX, XXX−XXX

(101) Singh, M. K. Simulating Growth Morphology of Urea Crystals from Vapour and Aqueous Solution. *CrystEngComm* **2015**, *17*, 7731−7744.

https://doi.org/10.1021/acsearthspacechem.3c00210
ACS Earth Space Chem. XXXX, XXX, XXX−XXX